

Scaling of Planar Sodium-Nickel Chloride Battery Cells to 90 cm² Active Area

T. Lan⁺^[a] E. Svaluto-Ferro,^[a] N. Kovalska,^[a] G. Graeber⁺⁺^[a] F. Vagliani,^[b] D. Basso,^[b] A. Turconi,^[b] M. Makowska,^[c] G. Blugan,^[a] C. Battaglia,^[a, d, e] and M. V. F. Heinz^{*[a]}

High-temperature sodium-nickel chloride (Na–NiCl₂) batteries offer a competitive solution for stationary energy storage due to their long-term stability, high energy efficiency, and sustainable raw materials. However, scaling up this technology faces challenges related to the costly integration of tubular Na-β''-alumina ceramic electrolytes into hermetically sealed battery cells. Alternative cell designs with a planar Na-β''-alumina ceramic electrolyte have been a focus of research for many years, and a series of achievements were made on cell design, on reduction of the operating temperature, and on the analysis of electrochemical reaction mechanisms. However, the data

presented in these reports was derived from laboratory-scale cells with small area (1–5 cm²). To date, there has been no research conducted on enlarging planar cells to an economically viable size. Here we report the fabrication of large planar Na-β''-alumina electrolytes and their integration into planar Na–NiCl₂ cells with 90 cm² active area and >7 Ah capacity. Our cell design enabled cycling at 300 °C for three months, transferring a cumulative capacity of 323 Ah. We discuss design and engineering considerations for large planar high-temperature cells emphasizing the need for cell stacking to compete with tubular Na–NiCl₂ batteries in terms of mass-specific energy.

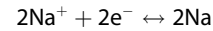
Introduction

In order to provide continuous power from intermittent renewable energy sources, stationary energy storage has recently become a focus.^[1–4] A clean, efficient, and safe technology, high-temperature sodium-nickel chloride (Na–NiCl₂) batteries are a promising solution for stationary energy storage. The design of commercial Na–NiCl₂ cells is based on a tubular solid electrolyte, made of ceramic Na-β''-alumina (Na₂O·xAl₂O₃).^[5–7] The inside of the Na-β''-alumina tube is filled with the solid

positive electrode composite, which consists of granules (Ni, Fe, NaCl, and additives) immersed in a secondary molten salt electrolyte (NaAlCl₄).^[5, 8] Na–NiCl₂ batteries are assembled in the discharged state, without active material in the negative electrode: the negative electrode, molten Na, is generated electrochemically upon maiden (first) charge on the outer surface of the Na-β''-alumina tube, where it is evenly distributed by a porous carbon wetting layer and metal shims, preventing dewetting of molten Na from the Na-β''-alumina surface.^[5, 9] The cell electrochemistry is based on the following reactions at 300 ± 40 °C: at the positive electrode:



at the negative electrode:



This provides a cell voltage of 2.57 V for the Ni reaction, and a cell voltage of 2.32 V for Fe the iron reaction.^[5, 10–11] Commercial Na–NiCl₂ cells with optimized design have a low cell resistance (< 4 Ω cm²) at a high areal capacity of ~150 mAh/cm², achieving energy efficiencies of approximately 90% for charge and discharge rates of ~C/8 and D/3, respectively.^[11–15] Industrial manufacturing and cell assembly processes provide durable hermetic seals and an efficient management of the molten phases.^[5, 12] However, production costs of the tubular high-temperature cells with their complex and costly three-dimensional design are relatively high, compared to lithium-ion batteries. Costs of high-temperature sodium-nickel chloride battery packs currently amount to 300–350 \$/kWh, resulting in overall energy costs of 0.07–0.08 \$/kWh/cycle, considering a design life of 4500 cycles.^[15]

[a] T. Lan,⁺ E. Svaluto-Ferro, N. Kovalska, G. Graeber,⁺⁺ G. Blugan, C. Battaglia, M. V. F. Heinz
Empa, Swiss Federal Laboratories for Materials Science and Technology,
Ueberlandstrasse 129, 8600 Dübendorf, Switzerland
E-mail: Meike.Heinz@empa.ch

[b] F. Vagliani, D. Basso, A. Turconi
FZSonic S.A., Via Laveggio 15, 6855 Stabio, Switzerland

[c] M. Makowska
Paul Scherrer Institut, Forschungsstrasse 111, 5232 Villigen PSI, Switzerland

[d] C. Battaglia
ETH Zurich, Department of Information Technology and Electrical Engineering,
Gloriastrasse 35, 8092 Zürich, Switzerland

[e] C. Battaglia
EPFL, School of Engineering, Institute of Materials, Station 1, 1015
Lausanne, Switzerland

[+] Current address: Materials Genome Institute, Shanghai University, Shanghai
200444, China

[+] Current address: Department of Chemistry, Humboldt-Universität zu Berlin
12489, Berlin, Germany

[] Supporting information for this article is available on the WWW under
<https://doi.org/10.1002/batt.202400447>

[] © 2024 The Authors. Batteries & Supercaps published by Wiley-VCH GmbH.
This is an open access article under the terms of the Creative Commons Attribution Non-Commercial License, which permits use, distribution and reproduction in any medium, provided the original work is properly cited and is not used for commercial purposes.

A planar cell design has been proposed to make the production of Na–NiCl₂ batteries, and of sodium-metal chloride cells in general, more compatible with automated mass production and quality control routines, thereby facilitating scale-up.^[11, 16–28] In addition, a planar cell design offers great flexibility, being able to accommodate variable active and passive components, enabling research on optimized sodium-metal chloride cell components and on electrochemical mechanisms.^[9–11, 29–30] Still, the making of reliable high-temperature cells with reproducible cycling performance is challenging. Various morphologies and chemical compositions of active materials have been studied at intermediate temperatures $\leq 200^{\circ}\text{C}$ in laboratory-scale cells with planar design (1–5 cm² active area) and moderate areal capacity (<60 mAh/cm²).^[18, 20, 22, 24, 26, 28, 31–37] Only few research studies report cycling data at 280–300 °C in planar^[10–11, 19, 28, 34, 38] or tubular^[15, 39–42] sodium-metal chloride cells. Operation at higher temperatures is of advantage as this decreases the cell resistance, thereby enhancing the energy efficiency of the battery.^[11] Furthermore, a high areal capacity is important to reduce cell production costs for stationary energy storage applications. In our recent work, we successfully increased the areal capacity of planar cells operated at 300 °C to the commercially viable level of 150 mAh cm⁻² in small cells with 3 cm² active area.^[11] Enlarging the cell area is a next step towards a possible commercialization of the planar design, but this comes with a number of additional challenges. Firstly, a planar Na- β'' -alumina electrolyte of corresponding dimensions and high quality is required. Mechanical stresses exerted on the ceramic electrolyte during cell cycling are substantially higher in planar cells, compared to tubular ones of the same areal capacity.^[14, 43] Secondly, planar cells require longer seals, compared to tubular cells. The tubular electrolyte in commercial cells is sealed along its narrow open end, while the sealing length spans the full outer circumference of the electrolyte in planar cells.^[5, 12, 15] Apart from technical difficulties, this increases cost and mass of passive components in planar cells. Thirdly, geometrical variations and dimensional tolerances of the cell components, in particular of sintered ceramic parts, hinder precise fittings, sealing, and an efficient management of molten NaAlCl₄ and Na in the cells. This is already very challenging in smaller lab cells but becomes more difficult with increasing diameter.^[10–11]

In this study, we present planar high-temperature Na–NiCl₂ battery cells with 90 cm² active area and 80 mAh cm⁻² areal capacity (0.5 g cm⁻² mass loading). In terms of active area, this represents an order of magnitude enhancement versus the state of the art in planar cells. To supply suitable planar ceramic electrolytes, we developed scalable shaping and sintering procedures for Na- β'' -alumina. These electrolytes were integrated into planar battery cells, which were cycled up to three months, transferring a total cumulative capacity of 323 Ah in more than 70 cycles. Efficient management of molten and corrosive NaAlCl₄ and Na within the cells at high active area is challenging and needs further refinements, in order to enhance cycle life and increase charge/discharge rates. In addition to the manufacturability of the electrolyte, we compare planar and state-of-the-art tubular cell designs in terms of their specific

energy density on cell level. Thereby, we provide a perspective on how planar high-temperature Na–NiCl₂ batteries may achieve competitive energy density by cell stacking.

Experimental Details

Planar high-temperature cells with 90 cm² active area comprise a ceramic subassembly consisting of a planar Na- β'' -alumina disc and ledged α -alumina collar, into which the positive electrode materials are filled on one side, while Na is generated on the other side during charge (see Figure 1).

Planar Electrolytes

Planar electrolyte discs of 11 cm diameter, ~95 cm² active area were prepared from spray-dried Li-stabilized Na- β'' -alumina powder.^[10–11, 44–45] Two different shaping and sintering procedures were developed to obtain robust ceramic electrolyte discs, which were based on tape-casting and die-pressing, respectively.

For tape-casting, slurry batches of ~345 g were prepared with the following composition (in wt. %):

49.3% Na- β'' -alumina powder, 6.7% poly (methyl methacrylate), 2.9% di-butyl phthalate, 2.9% PEG 300, 12.5% EtOH (99%), 25.7% 2-butanone. Tapes were cast on a support film at a doctor blade gap height of 250 ± 50 µm (CAM-T0, Keko Equipment, Slovenia) and dried in air at room temperature for a minimum of 24 hours. This resulted in green tapes of approximately 200–250 µm thickness, from which green discs of 140 mm diameter were punched out. After removal of the support film, 16–18 green discs were stacked in a steel mold, heated at 100 °C overnight, and laminated at a force of 1000 kN (650 bar).

Debinding and sintering of laminated green bodies was performed in a Nabertherm HT 40/17 furnace. To limit evaporation of Na₂O from Na- β'' -alumina during sintering,^[46] the green discs were placed inside MgO spinel crucibles with lid (Morgan Haldenwanger, Germany, inner diameter 150 mm). In contrast to previous studies,^[44–46] addition of a Na- β'' -alumina support powder below the green body was omitted to avoid cracking of the large discs (see supporting information (SI), Figure S1). Instead, the MgO crucibles were subjected to several sintering steps with Na- β'' -alumina before use, to avoid further uptake of Na₂O. The following heating and cooling program was applied for debinding and sintering of laminates (duration 80 h in total):

Heating to 200 °C at 0.16 °C min⁻¹, 2.5 h dwell time; heating from 200 °C to 500 °C at 0.25 °C min⁻¹; heating from 500 °C to 1000 °C at 3 °C min⁻¹, 2 h dwell time; heating from 1000 °C to 1600 °C at 0.6 °C min⁻¹, 5 min dwell time; 62 h in total. Cooling to ambient temperature at 1.5 °C min⁻¹, 18 h.

For die-pressing, 130–150 g of Na- β'' -alumina powder was uniaxially compacted at 1.3 kbar in a cylindrical die of 140 mm diameter for 1–1.5 min. The green disc was extracted from the die by inverting its assembly and sliding down the outer part. Sintering was performed with the green discs placed inside MgO spinel crucibles with lid as described for laminates above, but with reduced heating and cooling rates and dwell times (duration 35 h in total):

Heating to 200 °C at 0.5 °C min⁻¹, 2.5 h dwell time; heating to 500 °C at 0.5 °C min⁻¹; heating from 500 °C to 1000 °C at 3 °C min⁻¹, 2 h dwell time; heating 1000 °C to 1600 °C at 3 °C min⁻¹, 5 min dwell time; 27 h in total. Cooling to ambient temperature at 3 °C min⁻¹, 9 h.

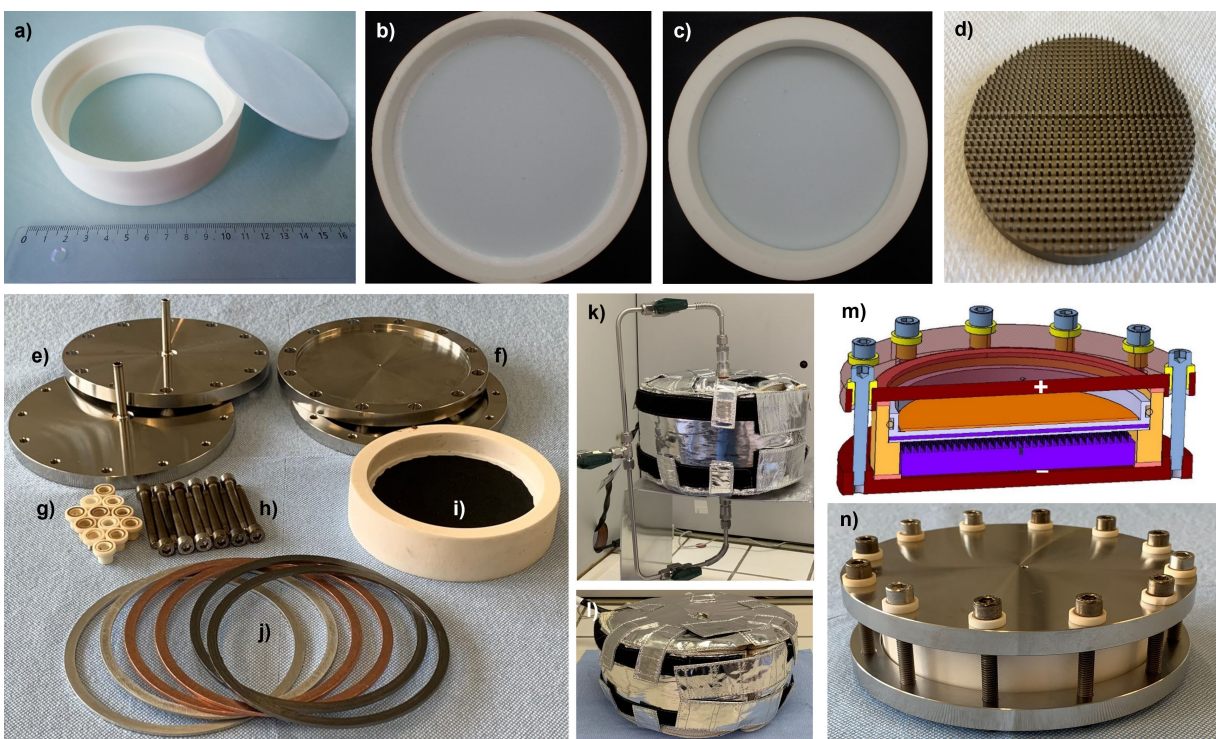


Figure 1. Components and design of planar sodium–metal chloride cells with 90 cm² active area. a) Insulating α -alumina collar with inner ledge to hold the Na- β'' -alumina disc. b) Top-view on the ceramic subassembly, showing the positive electrode compartment, and the glass-seal between α -alumina and Na- β'' -alumina. c) Bottom-view on the ceramic subassembly, showing the negative electrode compartment. d) Negative current collector. e) Endplates with welded tubes for vacuum infiltration. f) Endplates for cell testing. g) Insulating α -alumina washers. h) Bolts for cell closure. i) Ceramic subassembly with carbon-coated Na- β'' -alumina electrolyte disc on side of the negative electrode. j) Al, Cu, and graphite O-rings to seal the ceramic subassembly to the endplates; graphite O-rings were used for the cell presented here. k) Heated setup for vacuum infiltration of the positive electrode with molten NaAlCl₄. l) Heating jacked to control the cell temperature during cycling. m) Schematic cross-section and n) picture of planar high-temperature Na–NiCl₂ cell.

To characterize Na- β'' -alumina electrolytes, we measured their ion conductivity using impedance spectroscopy. Rectangular sections of the large electrolyte discs were contacted by Pt-wire electrodes at fixed distances of 5 mm–6 mm–5 mm in a four-probe geometry. At frequencies ≥ 1 kHz, the phase angles were close to 0. As discussed in more detail in previous studies,^[44, 47] the modulus of impedance $|Z|$ corresponds to the total resistance of the ceramic Na- β'' -alumina electrolyte in this case. Since the electronic conductivity of Na- β'' -alumina is negligible (e.g., 10⁻⁹ S cm⁻¹ at 60 °C),^[48] we derived the ion conductivity from $|Z|$ at 1 kHz using the sectional area of the rectangular sample (A) and the distance between inner electrodes l as $\sigma = \frac{l}{|Z|} \frac{1}{A}$. The content of Na₂O was determined from the weight change of samples immersed in molten AgNO₃ by Ag-ion exchange.^[44, 46, 49] Spatially resolved analysis of crystalline phases was performed over the thickness of Na- β'' -alumina electrolytes using XRD-contrast microscopy at the microXAS chemical imaging beamline at the Swiss Light Source (PSI).^[50] The data was acquired using the Dectris Eiger 4 M single photon counting detector,^[51] during a raster scan over cross sections of the ceramic samples. The measurement was performed with an X-ray beam with energy of 17.2 keV focused down to 1 μ m. The sample manipulator was moving the sample in the plane normal to the beam over the selected area with a step size of 10 μ m (both in x and y) and an acquisition time of 200 ms for each step. A more detailed description of the experimental and data processing procedures was reported previously.^[52]

Ceramic Subassembly and Design of Negative Electrode Current Collector

To electrically isolate the Na- β'' -alumina electrolyte discs from the cell's steel case, and to host anode and cathode materials in a ceramic subassembly, we designed monolithic α -alumina collars with an inner ledge (L-shaped inner profile, Figure 1a–c). The α -alumina collars were first ordered at Almath crucibles, UK, where a cost-efficient combination of slip-casting and sintering was applied to produce samples with middle (upper inner) diameters (MD) of 112 ± 1 mm, and (lower) inner diameters (ID) of 102 ± 1 mm, see Figure S2 in SI. However, the typical tolerances resulting from slip casting at these dimensions negatively affect the management of molten phases at the electrodes during pilot cell cycling. To obtain α -alumina collars with tighter tolerances, α -alumina cylinders were further obtained from Metoxit AG, Switzerland, who produced the pieces by powder pressing, green machining, and sintering with MD = 112.4 ± 0.2 mm (active area in upper cathode compartment 99 cm²) and ID = 101.5 ± 0.2 mm (active area in lower anode compartment 81 cm²). The cell cycling results presented here were obtained with the latter, with a corresponding average active cell area of 90 cm². A high-temperature glass seal¹⁰ was deposited on the inner ledge of α -alumina collars. After drying for 1–2 h, a planar Na- β'' -alumina electrolyte disc was inserted into the collar, and the subassembly was cured at 1050 °C. The quality of the ceramic subassembly was tested by isopropanol penetration, and a second sealing procedure was applied in case of leakage. Last but not least, a carbon coating was applied to the Na- β'' -alumina surface at the side for the negative electrode, to prevent dewetting of the molten sodium during cycling (Figure 1i). A suspension of 7 wt.%

carbon black, 11 wt.% sodium hexamethaphosphate, 55 wt.% isopropanol, 27 wt.% water, and 0.3 wt.% acetone was sprayed on the lower side of the Na- β'' -alumina in the ceramic subassembly using an airbrush system (Aztek, \approx 2 bar pressurized air); it was dried in air (Carbolite CWF 1200, $5^{\circ}\text{Cmin}^{-1}$ to 280°C , 5 min dwell time).^[9]

The negative current collector (Figure 1d) features a corrugated design, which proved to be effective in managing the molten Na with good capacity retention and low resistance in smaller cells.^[11] Corrugated current collectors were machined from aluminum (diameter 100 mm, 4 mm height) to obtain square columns with 1 mm side length and 3 mm height, spaced apart by 2 mm. These current collectors were subsequently anodized to provide a sodiophobic aluminium oxide finish and to enhance the mechanical stability at elevated temperatures. Disc-shaped current collectors (for the positive electrode) were made of Ni (diameter 110 mm).

Positive Electrode and Cell Assembly

The positive electrode consists of millimeter-sized cathode granules of Ni (50.4 wt.%, filamentary Ni255), Fe (6.6 wt.%), NaCl (39.0 wt.%), and additive powders (Al 0.5 wt.%, FeS 1.6 wt.%, NaF 1.5 wt.%, NaI 0.4 wt.%), fabricated using a roller press (Komarek B050 A, roll force 30 kN) and a granulator (Komarek G100SA). This mixed Ni/Fe electrode composition can deliver a reversible electrode capacity of 159 mAh g^{-1} (100% state of charge, SOC), with 60% SOC from Ni de/chlorination at 2.57 V, and 40% from Fe at 2.32 V.^[10] In the electrode granules, an overall active metal content of 30 wt.% (Fe 100% active, Ni 20.7% active) participates in electrochemical reactions during charge and discharge; 11.4% NaCl is used for irreversible chlorination of Al (33 mAh g^{-1}).

The battery cells with 0.5 g cm^{-2} mass loading were assembled inside an Ar-filled glovebox with both H_2O and O_2 levels below 0.1 ppm. 45 g granules, providing an irreversible capacity of 1.5 Ah and a reversible capacity of 7.2 Ah, were filled into the ceramic subassembly (on the upper side without carbon coating). Different from previous reports on smaller cells, we developed a vacuum infiltration system which provides a symmetric under pressure to both sides of the Na- β'' -alumina electrolyte for infiltration with the secondary electrolyte, molten NaAlCl₄. For this, we used stainless steel endplates with welded tubes during cell fabrication (Figure 1e). 45 g NaAlCl₄ was infiltrated into the granules at a pressure of $< 10 \text{ mbar}$ at 200°C (Figure 1k). For cell cycling, the endplates were exchanged by bare stainless-steel endplates (Figure 1f). A piece of Ni foam (Goodfellow, 1.6 mm thickness, 95% porosity) and additional 10 g of NaAlCl₄ were placed on top of the positive electrode for both electronic and ionic contact of the electrode composite, as reported previously.^[10–11] A small piece of thin Na foil ($\approx 20 \text{ mm}$ diameter round disc, $\approx 0.3 \text{ g}$) was placed between the carbon coated Na- β'' -alumina and the negative current collector to provide electrical contact and facilitate the first (maiden) charge. The current collectors were connected to the endplates mechanically by springs, and electrically by Ni wires and screws. Carbon felt strips (Sigratherm KFD 2) were placed above the current collector at the positive side as a buffer. To close the cell, the endplates were compressed against the ceramic subassembly by 12 steel bolts (Figure 1h), which were inserted in α -alumina washers (Figure 1g) to provide an electrical insulation between positive and negative electrode. To seal the electrode compartments, O-rings of different compositions can be applied, i.e., made from Al, Cu, or graphite (Figure 1j). We used graphite O-rings for the cycling results presented below.

A resistive heating jacket was designed to control the cell temperature (Figure 1l). Figure 1m provides a computer-aided design rendering of

the inner cell components, including a Ni current collector for the positive electrode and an Al current collector for the negative electrode. These were connected to the battery testing system through the conducting end plates via Ni cables. Finally, Figure 1n provides a picture of the planar large-area cell.

Cell Cycling

The large planar Na-NiCl₂ cells were electrochemically cycled inside the resistive heating jackets placed inside an Ar-filled glovebox. The charge-discharge behavior of the cells was characterized using a potentiostat (Biologic SP150) coupled to a 20 A current booster at $300 \pm 10^{\circ}\text{C}$. We applied a coupled constant-current and constant-voltage cycling routine (CC-CV) for cell cycling, like in commercial Na-NiCl₂ batteries. A constant-current (CC) was applied between 1.8 and 2.72 V. This was followed by constant-voltage (CV) soaking at 2.72 V at the end of charge, and at 1.8 V at the end of discharge, with capacity limitations to cycle the cell between 0% and 80% state-of-charge (SOC). Cells were charged/discharged at a given CC (up to 20 mA cm^{-2} , C/4) until the upper/lower cut-off voltage was reached. Then, CV charging/discharging was applied until the capacity limit was reached, or the current dropped below 0.2 mA cm^{-2} .

We derive the average cell resistance

$$R_{\text{avg}} = \frac{V_{\text{eq}}(1 - \eta_{\text{energy}})}{I_{\text{charge}}^* \eta_{\text{energy}} + I_{\text{discharge}}}$$

from the energy efficiency η_{energy} at a given charge/discharge current density $I_{\text{charge}}^*/I_{\text{discharge}}$, assuming an equilibrium voltage V_{eq} of 2.49 V .^[11]

Results and Discussions

Planar Electrolytes

The procurement of Na- β'' -alumina electrolytes of sufficient size and with high planarity is a prerequisite for the design of large planar sodium-metal chloride battery cells. While we previously presented tape-casting of Na- β'' -alumina solid electrolytes with 11 cm diameter,^[45] reproducible fabrication of large ceramic electrolytes without warping turned out to be challenging, and crack formation upon sintering lead to high scrap rates in some batches. To enhance fabrication yield and planarity of large Na- β'' -alumina discs prepared by tape-casting, we modified the sintering procedure in two aspects. First, we omitted the use of additional Na- β'' -alumina powder as sintering support. Second, we prolonged the debinding and sintering times from a total of previously 35 h to 80 h (see experimental details). This procedure enabled reproducible preparation of flat and crack-free electrolyte discs with diameter of $109.5 \pm 0.5 \text{ mm}$, and 1.5 to 1.8 mm thickness. In parallel, we prepared Na- β'' -alumina electrolytes by die-pressing, which were successfully sintered during 35 h. The resulting Na- β'' -alumina discs were flat and crack-free with a diameter of $111.5 \pm 0.3 \text{ mm}$, but with a higher thickness of 2–3 mm. The die-pressed samples were surface-ground to a thickness of $1 \pm 0.2 \text{ mm}$, resulting in a weight of $\sim 32 \text{ g}$ (volumetric density $\sim 3.3 \text{ g cm}^{-3}$, in-line with the theoretical density of Na- β'' -alumina, 3.27 g cm^{-3}).

The Na- β'' -alumina electrolytes prepared by both methods have very similar properties: Their ionic conductivity (measured in 4-probe geometry on disc fragments) amounts to 0.17–0.19 S cm⁻¹ at 300 °C, in line with previous reports on smaller samples.^[44, 53] Furthermore, the crystalline composition of both tape-cast and die-pressed electrolytes is constant over the sample thickness, as identified by crystalline phase mapping based on scanning micro-XRD imaging. As shown in Figure 2, the major crystalline phase present is Na- β'' -alumina (space group R-3 m H, 93–94 wt. %), with minor amounts of sodium aluminate as a second phase (NaAlO₂, space group P 41212, 6–7 wt. %). The refined c-lattice parameter of Na- β'' -alumina amounts to 33.50–33.51 Å. Details on the phase content and crystal lattice parameters from Rietveld refinements are summarized in the SI in Table S1, Figure S3, and Figure S4. The Na₂O content of Na- β'' -alumina $X_{\text{Na}_2\text{O}}$ as measured by Ag-ion exchange, is 9.8–9.9 wt. % for both types of samples. This is in-line with previous results, according to which $X_{\text{Na}_2\text{O}}$ can be estimated from its c-lattice parameter l_c .^[46]

$$X_{\text{Na}_2\text{O}}(\text{wt. \%}) = (-4.21 \pm 0.43)^* l_c(\text{\AA}) + (150.5 \pm 14.4)$$

Both tape-casting and die-pressing are scalable shaping techniques. At this stage, tape-casting requires a higher number of processing steps and significantly longer debinding and sintering times, due to the higher amount of the polymeric components in the slurry preparation. When punching circular shapes from tapes, it is essential to manage the resulting scrap material efficiently. Die-pressing enables the use of a faster sintering program, while subsequent surface grinding assured reproducible planarity. However, the diamond grinding process is both cost- and energy-intense. The implementation of a floating die press method (widely

used in the ceramic industry) provides an alternative capable of directly achieving the required thickness of 1 mm, without the need for additional post-machining.

In this study, we selected large Na- β'' -alumina electrolytes prepared by die-pressing for integration into high-temperature battery cells.

Cell Cycling

Based on our previous planar sodium-metal chloride cell design with 3 cm² active area, we scaled all components to a planar cell with 90 cm² active area.^[9–11, 29–30] Instead of using two α -alumina collars, we adopted a monolithic α -alumina insulator with an inner ledge (Figure 1). This avoids gas leakage to and from the outside environment at the glass seal (between α -alumina insulator and Na- β'' -alumina electrolyte) and reduces cost and weight by reducing the number of seals. The cell presented here has a mass loading of 0.5 g cm⁻² (relative to the mass of both electrodes). Based on the cathode composition, it provides a theoretical reversible capacity of 7.2 Ah (100% SOC, 159 mAh g⁻¹, 80 mAh cm⁻²). To investigate the influence of charge/discharge rates on available capacity and energy efficiency, we varied the current density applied during capacity-limited CC–CV cycling. The initial performance of the large-area planar cell is summarized in Figure 3 (cycles 1–21, after maiden cycle 0). Figure 3a shows the evolution of cell voltage at variable current densities. Typical for Na–NiCl₂ cells with a mixed Ni/Fe electrode, the voltage profiles exhibit hysteresis between charge and discharge, caused by additional overpotentials effective during charge. This is ascribed to electrochemical reactions of additives (e.g., FeS, NaF, NaI) and to formation of intermediate phases upon

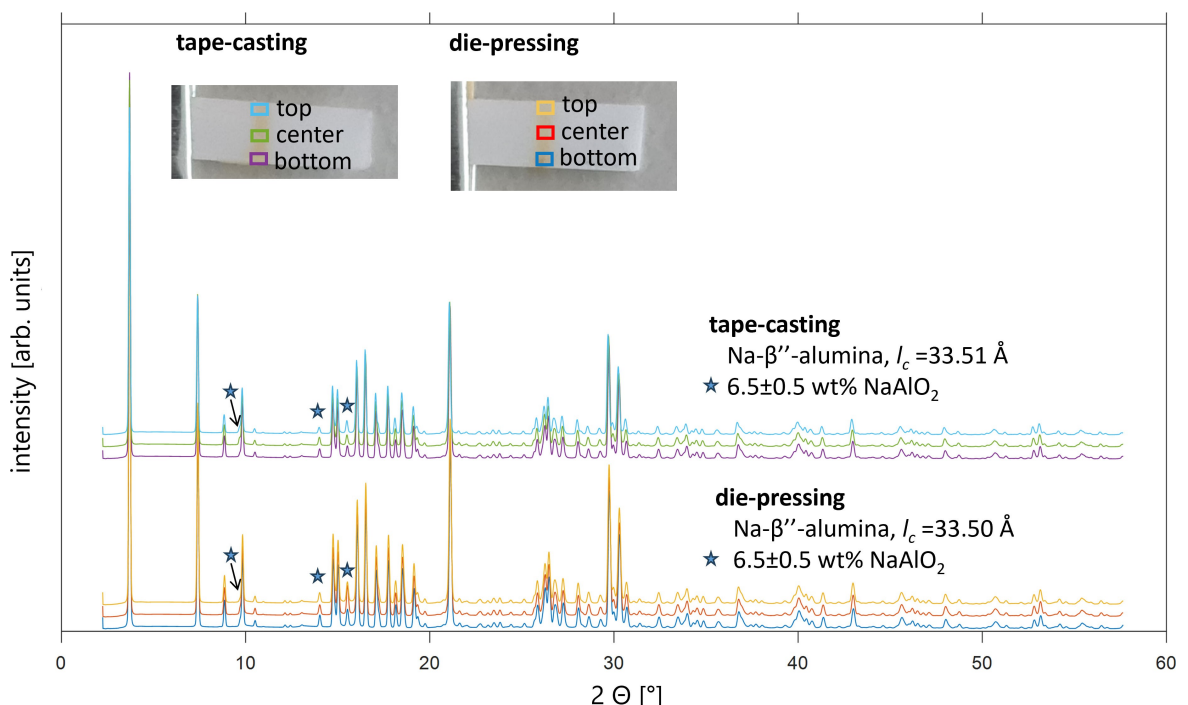


Figure 2. X-ray diffraction patterns obtained from selected regions within the thickness of Na- β'' -alumina electrolytes (top, center, bottom, as shown in the insets).

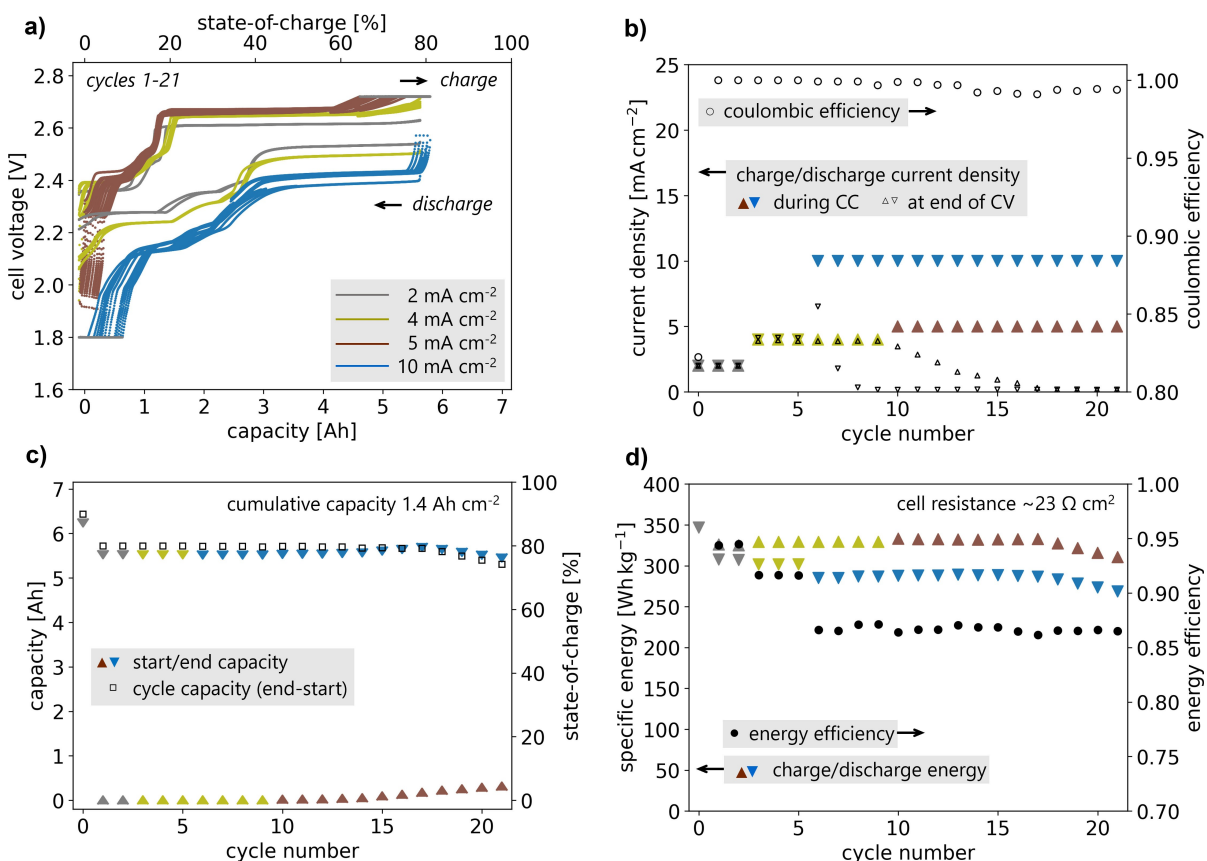


Figure 3. First cycles of a planar sodium-metal chloride cell with 90 cm² active area at 300 °C. a) Evolution of cell voltage at current densities between 2 and 10 mA cm⁻². b) Current density applied during charge/discharge, and corresponding coulombic efficiency. The large, solid arrows indicate the current density applied during CC charge/discharge, while the small, open arrows display the reduced current density reached at the end of CV charge/discharge. c) Start/end capacity and cycle capacity with cycle number. d) Specific energy during charge/ discharge (relative to the mass of both electrodes), and corresponding energy efficiency per cycle. The corresponding cell resistance is stable at ~23 Ω cm² in cycles 6–21. A discharge energy of 288 Wh kg⁻¹ is obtained at 10 mA cm⁻² (C/8) at an energy efficiency of 87%.

charge, which undergo chemical reactions before discharge (e.g., $\text{Na}_6\text{FeCl}_8 \rightarrow 6\text{NaCl} + \text{FeCl}_2$).^{[5, 10–11, 54] The voltage evolution during discharge aligns with the composition of cathode granules, and with previous studies: the voltage plateau above 40% SOC corresponds to Ni de-chlorination, while Fe de-chlorination, combined with the contribution of additives and intermediate phases, influences the cell voltage below 40% SOC.^[10–11] The different charge/discharge current densities applied during CC, the current density at the end of CV, and the coulombic efficiency per cycle are displayed in Figure 3b. For the first 15 cycles, the cell reaches the capacity limit of 5.7 Ah (80% SOC) at current densities between 2 and 10 mA cm⁻², with a coulombic efficiency equal or very close to 100%. As a result, stable cycling is achieved between 0 and 80% SOC (Figure 3c). The discharge energy is 307 Wh kg⁻¹ at 2 mA cm⁻², and 288 Wh kg⁻¹ at 10 mA cm⁻² (C/8), relative to the mass of both electrodes (Figure 3d). Energy efficiencies of 87% in cycle 5–21 correspond to a stable cell resistance of ~23 Ω cm² in cycles 6–21 (see SI, Figure S5a).}

However, during subsequent cycles, the accessible capacity fades continuously, even though the cell voltage remains relatively stable. This is shown in Figure 4a for cycles 25–55 and 56–76 at charge current densities of 7 mA cm⁻² (C/11) and discharge current densities of 7 mA cm⁻² and 20 mA cm⁻² (C/4), respectively. Although

the coulombic efficiency did not decrease continuously with cycle number but merely scattered around 100% SOC (at 99.5 ± 0.3%, Figure 4b), the cycle capacity decreased significantly, from 80% SOC (5.7 Ah) to 30% SOC (2.2 Ah). Figure 4c summarizes the capacity evolution over almost 80 cycles, which results in a cumulative half-cycle capacity of 323 Ah, 3.6 Ah cm⁻². Related to capacity limitations upon discharge, the start capacity increases from 0% SOC to 16% SOC after the first 15 cycles. The end capacity, associated with capacity limitations upon charge, decreases significantly, from 80% SOC to 46% SOC. The decrease in cycle capacity induced a significant decrease in specific discharge energy (Figure 4d). However, the energy efficiency remained relatively stable at a given set of charge/discharge current densities: >85% energy efficiency for charge/discharge at 7 mA cm⁻² (cycles 25–55), and >76% energy efficiency for charge at 7 mA cm⁻² and discharge at 20 mA cm⁻² (cycles 56–76). The cell resistance remained relatively stable at <30 Ω cm² for all subsequent cycles, even showing a tendency towards lower values for higher current densities (e.g. 23 Ω cm² in cycle 76, see SI, Figure S5b).

Post-mortem characterization after 79 cycles revealed a significant loss of molten NaAlCl₄ secondary electrolyte from the positive electrode compartment, together with some loss and oxidation of sodium from the negative electrode compartment. Previous reports

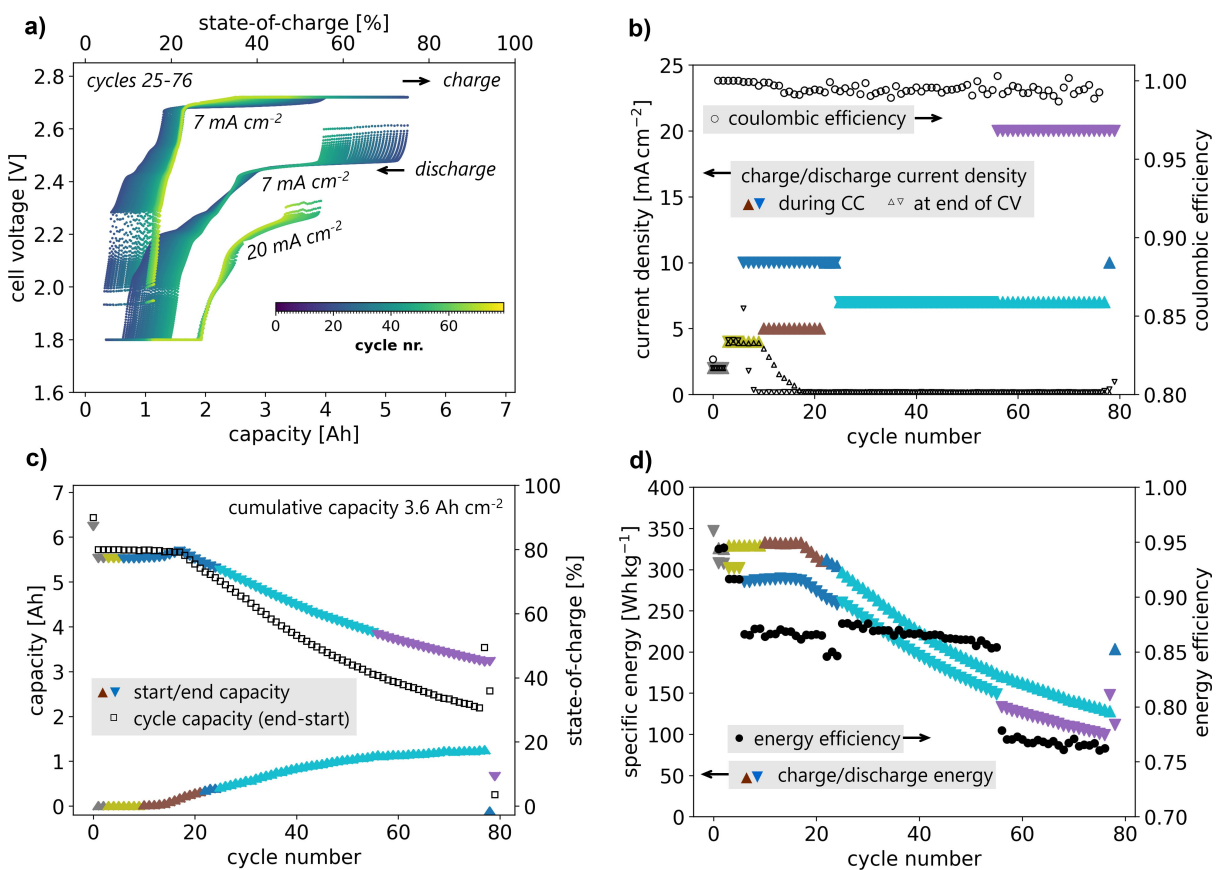


Figure 4. Extended cycling of the same planar sodium–metal chloride cell with 90 cm² active area for ~80 cycles at 300 °C. a) Evolution of cell voltage in cycles 25–55 for charge/discharge at 7 mA cm⁻², and in cycles 56–76 for charge at 7 mA cm⁻², discharge at 20 mA cm⁻². b) Current densities of up to 20 mA cm⁻² are applied during charge/discharge. After cycle 15, the lower current limits are hit during CV charge/discharge, and the cycle capacity target (80% SOC, 5.7 Ah) is not fully reached. As a result, the coulombic efficiency decreases slightly, but remains ≥ 99% in all cycles. c) Start/end capacity and cycle capacity with cycle number. Capacity fading is associated with loss of molten NaAlCl₄ at the positive electrode, and with loss or oxidation of molten Na at the negative electrode. d) The specific charge/ discharge energies (relative to the mass of both electrodes) decrease after cycle 18 due to capacity fading. The energy efficiency remains > 85% at 7 mA cm⁻² (C/11), and > 76% at 7 mA cm⁻² charge, 20 mA cm⁻² discharge current density.

showed electrochemical decomposition of NaAlCl₄ to volatile AlCl₃ to occur in both planar and tubular Na–NiCl₂ cells within normal cycling conditions (e.g., ≤ 2.72 V),^[11, 55] which may induce NaAlCl₄ leakage. NaAlCl₄ leakage leads to a continuous reduction of cathode material volume that is wetted by NaAlCl₄, which is identified as a major cause of degradation for this cell. Efficient management of NaAlCl₄ was hindered by geometrical variations and dimensional tolerances of the large cell components. Especially, precise dimensions of the ceramic α-alumina collars were difficult to achieve, leading to up to 1 mm wide gaps between the ceramic α-alumina collar and the metal current collectors for both electrodes. Despite careful machining of the current collectors to precisely fit the α-alumina collars, the difference in thermal expansion coefficient and the large size induced high mechanical stress between the current collectors and the α-alumina collar, making the cell mechanically unstable. The performance of this large-area cell was thus dominated by insufficient management of molten NaAlCl₄ at the electrode. Nevertheless, at an active area of 90 cm², this cell transferred a cumulative capacity of 323 Ah, 3.6 Ah cm⁻² in ~80 cycles, representing the first electrochemical cycling results on large high-temperature Na–NiCl₂ battery cells. To further enhance the cycle life of planar high-temperature battery cells with large

active area, improving the sealing of electrode compartments is essential. This not only prevents the loss of NaAlCl₄ and sodium but also allows cells to be sealed at a reduced gas pressure, mitigating pressure differences during electrochemical cycling and temperature changes.^[14]

The design of planar high-temperature battery cells presented here is also not optimized for weight and volume, but instead facilitates cell dis-/assembly by the use of re-usable components at laboratory scale (see Figure 5 for a comparison of commercial tubular cells to small and large planar cells). The enlarged passive cell components further resulted in a higher cell resistance, compared to previous cells of smaller size (i.e., 23 Ω cm², compared to 3–6 Ω cm²).^[10–11] For commercialization, the cell design may be adopted to reduce cost, weight, and resistance of all passive components. In particular, the end plates can be replaced by sheet metal, a metal foam can replace the current collector at the negative electrode, the volume of the α-alumina ring can be drastically reduced, and the cell can be closed by combining glass seals and welding. The incorporation of temperature-resistant polymers as seals, or potentially replacing the insulating α-alumina collar, provides additional design options. In combination with optimized components and industrial fabrication processes, a planar

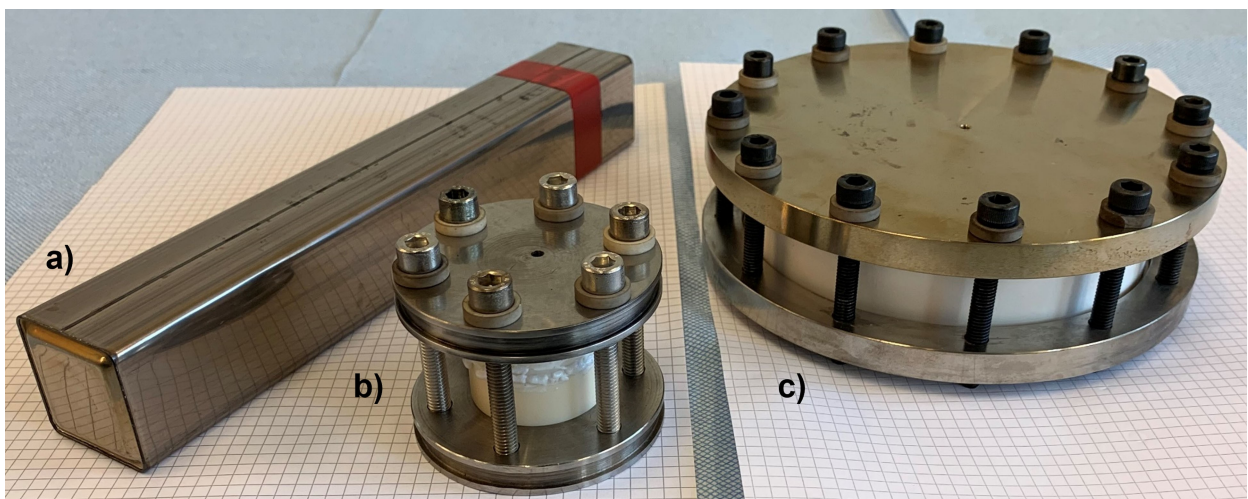


Figure 5. Comparison of different cell designs for high-temperature sodium–metal chloride batteries. a) Commercial tubular cell with 260 cm^2 active area. b) Planar cell with 3 cm^2 active area. c) Planar cell with 90 cm^2 active area.

design can benefit the scalability and mass-production of high-temperature Na– NiCl_2 battery cells, compared to the state-of-the-art tubular design.

Nevertheless, a planar cell design also introduces new challenges. For example, a planar geometry generally requires longer seals, a larger insulating collar, and a larger cell case. To evaluate the influence of passive components in an optimized planar cell design, we projected their weight from state-of-the art components applied in commercial tubular cells.

A summarized in Table 1, we classify cell components into two different types: core components and supporting components. The core components of a cell include the positive electrode materials (positive electrode and secondary electrolyte), whose weight is proportional to the capacity of the cell. Here, we consider the solid electrolyte as a core component, assuming a similar weight and thicknesses to assure mechanical stability. The negative electrode (Na) is generated electrochemically upon charge, and the handling of Na metal is not required during assembly of sodium–metal

chloride cells. For both planar and tubular designs with the same capacity, the core components are assumed to have the same volume and weight, though arranged in different geometries. In state-of-the-art tubular cells with a capacity of 38 Ah, the approximate weight of the core components is 490 g, including 365 g materials in the positive electrode and 125 g Na– β'' -alumina electrolyte. The supporting components include all the other components necessary for an operating cell, including current collectors, α -alumina insulators, cell case, and connecting parts. Minimizing cost and weight of the supporting components is very important to design cost-efficient cells with high cell-specific energy. In the tubular cells, the approximate weight of the supporting components is 200 g, including 55 g for the positive current collector, 30 g for the negative current collector, 30 g for α -alumina insulator, and 90 g for the sheet-metal cell case. In contrast to the corrugated current collector applied in our laboratory cell above, we assume an optimized planar design with current collectors of similar weight/volume as applied in the tubular design (e.g., made from sheet

Table 1. Comparison of component weights between a state-of-the-art tubular cell and an optimized planar cell (both with 38 Ah capacity).

Components		Tubular cell	Optimized planar cell
Core components (proportional to cell capacity)	granules (Ni, Fe, NaCl, additives)	250 g	250 g
	secondary electrolyte NaAlCl_4	115 g	115 g
	Na– β'' -alumina electrolyte	125 g	125 g
	current collector (positive)	55 g (Ni rod with carbon felt)	55 g (0.2 mm Ni sheet)
	current collector (negative)	30 g (0.1 mm steel sheet)	30 g (0.1 mm structured steel sheet)
	α -alumina insulator with sealing	30 g	45 g
	Cell case with electrical connectors	90 g (350 cm^2 surface area)	140 g (560 cm^2 surface area)
	Total	695 g	760 g

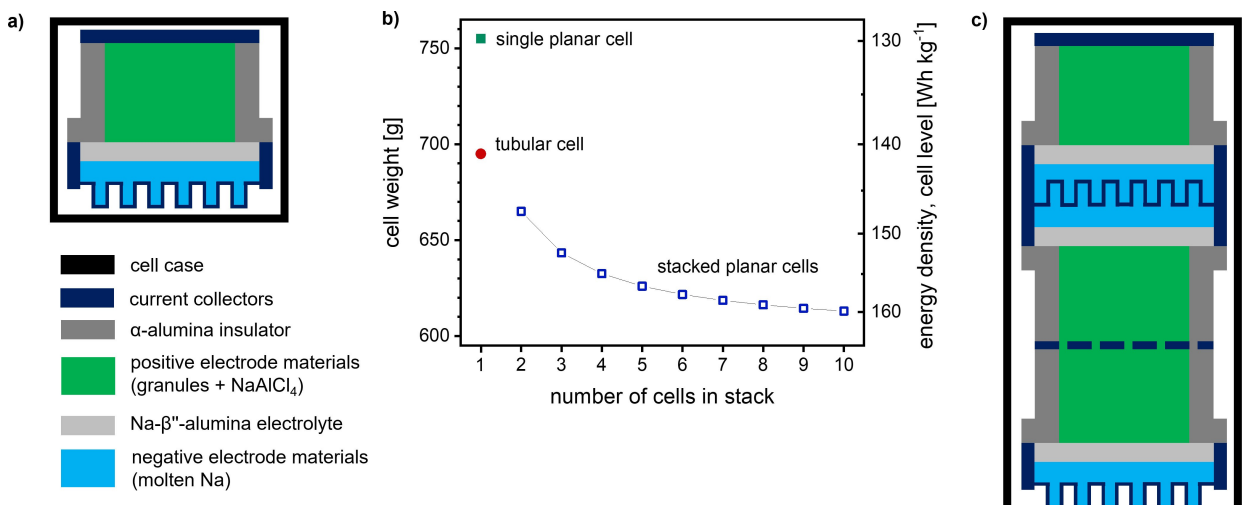


Figure 6. Stacking of cells. a) Sketch of single planar cell. b) Expected cell weight and energy density of single and stacked planar cells, compared to a state-of-the-art tubular cell with 38 Ah capacity. c) Sketch of stacked planar cells, with 3 cells connected as an example.

metal and metal foam or felt). However, the cell case for a single planar cell with cylindrical morphology has a much larger surface area of 560 cm^2 , compared to $\sim 350\text{ cm}^2$ in the state-of-the-art tubular design. Thus, an additional weight of 50 g results for the planar cell case. In addition, extra weight (e.g., +15 g) is expected for the α -alumina insulator covering the circumference of planar cells (Figure 6a). As a result, we expect a higher weight and lower cell-specific energy for a planar design of 38 Ah Na-NiCl₂ cells. As shown in Figure 6b, the increased contribution of α -alumina insulator and cell case increases the cell weight from 695 g to 760 g. Based on an equilibrium voltage of 2.58 V for nickel de-chlorination, this reduces the nominal cell-specific energy of 140 Wh kg^{-1} in state-of-the-art tubular cells to 130 Wh kg^{-1} for the optimized planar cell design.

However, a planar cell design provides the possibility cell stacking. By stacking two cells connected in parallel (Figure 6c), the weight of shared current collectors and cell cases is reduced, and the energy density of stacked planar cells would exceed that of tubular cells. Stacking of up to 10 cells could provide a cell-specific energy of up to 160 Wh kg^{-1} (Figure 6b), only based on a weight reduction of cell case and current collectors.

Conclusions

In summary, the present work reports the first electrochemical cycling results on large high-temperature Na-NiCl₂ battery cells, with an active area of 90 cm^2 and an areal capacity 80 mAh cm^{-2} . The cell presented here was cycled at current densities of up to 20 mA cm^{-2} during discharge and delivered a cumulative half-cycle capacity of 323 Ah, i.e., 3.6 Ah cm^{-2} , in ~ 80 cycles at 300°C . With these large-area cells, we identified difficulties in precisely controlling the dimension of the ceramic α -alumina collars as a main cause for the loss of molten NaAlCl₄, leading to capacity fading. A tight fit with the metal current collectors inside the α -alumina collar, however, leads to mechanical instability due to thermal expansion.

Further engineering enhancements are needed to solve these challenges. We further discussed the prospected cell-specific energy with optimized components and found that a single planar cell is not competitive in cell weight, compared to tubular cell with the same capacity. Increased weight in the planar cell comes from a larger α -alumina insulator, and from a cell case of increased surface area. Stacking of the planar cells, however, could reduce the cell-specific weight and therefore increase the specific energy to values better than those of present state-of-the-art tubular cells.

Highlights

- Large planar Na- β'' -alumina electrolytes prepared by tape-casting and die-pressing (11 cm diameter, $1\text{-}2\text{ mm}$ thickness).
- Scaled planar sodium-nickel chloride cells to 90 cm^2 active area with high capacity ($> 7\text{ Ah}$, 80 mAh cm^{-2}).
- Successful cell cycling at 300°C at rates up to C/4 (20 mA cm^{-2}), cumulative capacity 323 Ah (3.6 Ah cm^{-2}).
- Dimensional variations of the ceramic cell components impact molten material losses and cell ageing.

Acknowledgements

The authors thank Benjamin Kunz, Ardian Salihu, and Erwin Pieper for their help in designing and producing the high-temperature cell components. This work received funding from the Swiss Federal Office of Energy (SFOE) under contract number SI/501674, and from the European Union's Horizon 2020 research and innovation program under grant agreement No. 963599. Open Access funding provided by ETH-Bereich Forschungsanstalten.

Conflict of Interests

The authors declare no conflict of interest.

Data Availability Statement

The data that support the findings of this study are openly available in Zenodo at <https://doi.org/10.5281/zenodo.11126765>, reference number 11126765.

Keywords: alkali-metal anode • high-temperature ZEBRA batteries • molten-salt batteries • scalable stationary energy storage • Sodium-metal chloride batteries

- [1] D. Larcher, J. M. Tarascon, *Nat. Chem.* **2015**, *7*, 19–29, <https://doi.org/10.1038/nchem.2085>.
- [2] J. Wüllner, *Current Sustainable/Renewable Energy Reports* **2021**, *8*, 263–273, <https://doi.org/10.1007/s40518-021-00188-2>.
- [3] Z. Zhu, *Chem. Rev.* **2022**, *122*, 16610–16751, <https://doi.org/10.1021/acs.chemrev.2c00289>.
- [4] A. A. Kebede, T. Kalogiannis, J. Van Mierlo, M. Berecibar, *Renewable Sustainable Energy Rev.* **2022**, *159*, 112213, <https://doi.org/https://doi.org/10.1016/j.rser.2022.112213>.
- [5] J. L. Sudworth, *J. Power Sources* **2001**, *100*, 149–163, [https://doi.org/10.1016/S0378-7753\(01\)00891-6](https://doi.org/10.1016/S0378-7753(01)00891-6).
- [6] X. Lu, G. Xia, J. P. Lemmon, Z. Yang, *J. Power Sources* **2010**, *195*, 2431–2442, <https://doi.org/10.1016/j.jpowsour.2009.11.120>.
- [7] K. B. Hueso, M. Armand, T. Rojo, *Energy Environ. Sci.* **2013**, *6*, 734–749, <https://doi.org/10.1039/c3ee24086j>.
- [8] J. L. Sudworth, *J. Power Sources* **1994**, *51*, 105–114, [https://doi.org/10.1016/0378-7753\(94\)01967-3](https://doi.org/10.1016/0378-7753(94)01967-3).
- [9] D. Landmann, G. Graeber, M. V. F. Heinz, *Mater. Today* **2020**, *18*, 100515–100515, <https://doi.org/10.1016/j.mtener.2020.100515>.
- [10] G. Graeber, *Adv. Funct. Mater.* **2021**, *31*, 2106367–2106367, <https://doi.org/10.1002/adfm.202106367>.
- [11] T. Lan, *Adv. Funct. Mater.* **2023**, *33*, 2302040, <https://doi.org/https://doi.org/10.1002/adfm.202302040>.
- [12] C. H. Dustmann, *J. Power Sources* **2004**, *127*, 85–92, <https://doi.org/10.1016/j.jpowsour.2003.09.039>.
- [13] R. Benato, *J. Power Sources* **2015**, *293*, 127–136, <https://doi.org/10.1016/j.jpowsour.2015.05.037>.
- [14] M. V. F. Heinz, G. Graeber, D. Landmann, C. Battaglia, *J. Power Sources* **2020**, *465*, 228268–228268, <https://doi.org/10.1016/j.jpowsour.2020.228268>.
- [15] M. V. F. Heinz, *Electrochim. Acta* **2023**, *464*, 142881–142881, <https://doi.org/10.1016/j.electacta.2023.142881>.
- [16] X. Lu, *ECS Trans.* **2010**, *28*, 7–13, <https://doi.org/10.1149/1.3492326>.
- [17] X. Zhan, *Energy Storage Mater.* **2020**, *24*, 177–187, <https://doi.org/10.1016/j.ensm.2019.08.021>.
- [18] G. Li, X. Lu, J. Y. Kim, J. P. Lemmon, V. L. Sprenkle, *J. Mater. Chem. A* **2013**, *1*, 14935–14942, <https://doi.org/10.1039/c3ta13644b>.
- [19] X. Lu, *J. Power Sources* **2012**, *215*, 288–295, <https://doi.org/10.1016/j.jpowsour.2012.05.020>.
- [20] G. Li, *J. Power Sources* **2012**, *220*, 193–198, <https://doi.org/10.1016/j.jpowsour.2012.07.089>.
- [21] X. Zhan, *Adv. Energy Mater.* **2020**, *10*, <https://doi.org/10.1002/aenm.202001378>.
- [22] K. Jung, *J. Power Sources* **2018**, *396*, 297–303, <https://doi.org/10.1016/j.jpowsour.2018.06.039>.
- [23] H.-J. Chang, N. L. Canfield, K. Jung, V. L. Sprenkle, G. Li, *ACS Appl. Mater. Interfaces* **2017**, *9*, 11609–11614, <https://doi.org/10.1021/acsmami.7b00271>.
- [24] H. J. Chang, *Adv. Mater. Interfaces* **2018**, *5*, 1701592–1701592, <https://doi.org/10.1002/admi.201701592>.
- [25] H. Wang, C. Peng, *Sustain. Energy Fuels* **2023**, *7*, 330–354 <https://doi.org/10.1039/D2SE01525K>.
- [26] G. Li, *Adv. Energy Mater.* **2015**, *5*, 1500357–1500357, <https://doi.org/10.1002/aenm.201500357>.
- [27] G. Li, X. Lu, J. Y. Kim, J. P. Lemmon, V. L. Sprenkle, *J. Power Sources* **2014**, *249*, 414–417, <https://doi.org/10.1016/j.jpowsour.2013.10.110>.
- [28] G. Li, *J. Power Sources* **2014**, *272*, 398–403, <https://doi.org/10.1016/j.jpowsour.2014.08.106>.
- [29] D. Landmann, E. Svaluto-Ferro, M. V. F. Heinz, P. Schmutz, C. Battaglia, *Adv. Sci.* **2022**, *9*, e2201019, <https://doi.org/10.1002/advs.202201019>.
- [30] L. Sieuw, *Energy Storage Mater.* **2024**, *64*, 103077, <https://doi.org/https://doi.org/10.1016/j.ensm.2023.103077>.
- [31] H. J. Chang, *J. Power Sources* **2017**, *348*, 150–157, <https://doi.org/10.1016/j.jpowsour.2017.02.059>.
- [32] X. Lu, *J. Power Sources* **2017**, *365*, 456–462, <https://doi.org/https://doi.org/10.1016/j.jpowsour.2017.07.029>.
- [33] Y. Li, *Chem. Eng. J.* **2020**, *387*, 124059–124059, <https://doi.org/10.1016/j.cej.2020.124059>.
- [34] G. Li, *Nat. Commun.* **2016**, *7*, 10683–10683, <https://doi.org/10.1038/ncomms10683>.
- [35] X. Lu, *ACS Omega* **2018**, *3*, 15702–15708, <https://doi.org/10.1021/acsomega.8b02112>.
- [36] Y. Lee, *J. Power Sources* **2019**, *440*, 227110–227110, <https://doi.org/10.1016/j.jpowsour.2019.227110>.
- [37] X. Zhan, *Adv. Energy Mater.* **2020**, *10*, <https://doi.org/10.1002/aenm.201903472>.
- [38] S. M. Kim, *Bull. Korean Chem. Soc.* **2016**, *37*, 695–699 <https://doi.org/10.1002/bkcs.10756>.
- [39] B.-M. Ahn, *Batteries* **2022**, *8*, <https://doi.org/10.3390/batteries8100163>.
- [40] B. M. Ahn, *Materials* **2021**, *14*, <https://doi.org/10.3390/ma14195605>.
- [41] B. M. Ahn, *Composites Part B* **2019**, *168*, 442–447, <https://doi.org/10.1016/j.compositesb.2019.03.064>.
- [42] A. D. G. Lee, *Journal of Electrochemical Science and Technology* **2021**, *12*, 398–405, <https://doi.org/10.33961/JECST.2021.00059>.
- [43] K. Jung, *J. Power Sources* **2016**, *324*, 665–673, <https://doi.org/10.1016/j.jpowsour.2016.05.128>.
- [44] M. C. Bay, *ACS Appl. Energ. Mater.* **2019**, *2*, 687–693, <https://doi.org/10.1021/acsam.8b01715>.
- [45] S. C. Ligon, *Materials* **2020**, *13*, 433–433, <https://doi.org/10.3390/ma13020433>.
- [46] M. C. Bay, M. V. F. Heinz, A. N. Danilewsky, C. Battaglia, U. F. Vogt, *Ceram. Int.* **2021**, *47*, 13402–13408, <https://doi.org/10.1016/j.ceramint.2021.01.197>.
- [47] M. V. F. Heinz, M. C. Bay, U. F. Vogt, C. Battaglia, *Acta Mater.* **2021**, *213*, 116940–116940, <https://doi.org/10.1016/j.actamat.2021.116940>.
- [48] M. C. Bay, *Adv. Energy Mater.* **2020**, *10*, 1902899–1902899, <https://doi.org/10.1002/aenm.201902899>.
- [49] B. Dunn, B. B. Schwarz, J. O. Thomas, P. E. D. Morgan, *Solid State Ionics* **1988**, *28(30)*, 301–305, [https://doi.org/10.1016/S0167-2738\(88\)80054-7](https://doi.org/10.1016/S0167-2738(88)80054-7).
- [50] C. N. Borca, *J. Phys. Conf. Ser.* **2009**, *186*, 012003, <https://doi.org/10.1088/1742-6596/186/1/012003>.
- [51] I. Johnson, *Journal of Instrumentation* **2014**, *9*, C05032, <https://doi.org/10.1088/1748-0221/9/05/C05032>.
- [52] A. W. Colldeweih, M. G. Makowska, O. Tabai, D. F. Sanchez, J. Bertsch, *Materialia* **2023**, *27*, 101689, <https://doi.org/https://doi.org/10.1016/j.mtla.2023.101689>.
- [53] S. C. Ligon, *Solid State Ionics* **2020**, *345*, 115169–115169, <https://doi.org/10.1016/j.ssi.2019.115169>.
- [54] V. Zinth, *J. Electrochem. Soc.* **2015**, *162*, A384–A391, <https://doi.org/10.1149/2.0421503jes>.
- [55] T. Javadi, A. Petric, *J. Electrochem. Soc.* **2011**, *158*, A700–A700, <https://doi.org/10.1149/1.3574023>.

Manuscript received: July 1, 2024

Revised manuscript received: July 23, 2024

Accepted manuscript online: August 12, 2024

Version of record online: October 4, 2024